PNAS
www.pnas.org

Supplementary Information

Bioinspired underwater locomotion of light-driven liquid crystal gels

Hamed Shahsavan, Amirreza Aghakhani, Hao Zeng, Yubing Guo, Zoey S. Davidson, Arri Priimagi, and Metin Sitti

Corresponding author: sitti@is.mpg.de

This PDF file includes:

Supplementary Information
Figures S1 to S11
Tables S1 to S2
Legends for Movies S1 to S8
SI References

Other supplementary materials for this manuscript include the following:

Movies S1 to S8

www.pnas.org/cgi/doi/10.1073/pnas.1917952117

Supplementary Information

S1. Modeling of heat transfer in water and air

The photothermal heating of an LCN cantilever in air or water medium (shown in Fig. 2) was modeled in the Heat Transfer module of COMSOL Multiphysics 5.4. Following the Beer-Lambert law for the material heating due to light irradiation, the governing differential equation for the light intensity I is written as:

$$\frac{\partial I}{\partial z} = \alpha(T) I \ , \tag{S1}$$

where z is the direction along the incident beam, and $\alpha(T)$ is the temperature-dependent absorption coefficient of the material. We assumed that α is constant and its value was extracted from ref. (60). The temperature distribution within the control volume of the heated materials can be obtained by solving the following heat diffusion equation:

$$\rho C_p \frac{\partial T}{\partial t} - \nabla.(k \nabla T) = q_{source} \ , \tag{S2}$$

where ρ, C_p, and k are the density, specific heat, and thermal conductivity of the material, respectively(61). The first term on the left side is related to the total energy storage inside the material which leads to the overall temperature increase over time. $q_{source} = \alpha(T) I$ is the heat source, which implies the photothermal heating due to the light irradiation at a given surface of the control volume. A Dirichlet boundary condition was used to define the top surface on which the light beam is exposed with a Gaussian distribution. The diffuse surface boundary condition was employed to account for the heat radiation of the material, assuming the heated object as a gray body (surface emissivity of $= 0.8$). The radiation loss was assumed to follow the Stefan-Boltzmann law:

$$q_{rad} = \epsilon \sigma \left(T_{ambient}^4 - T_{surface}^4 \right) \ , \tag{S3}$$

where $\sigma = 5.67 \times 10^{-8}\ Wm^{-2}K^{-4}$ is the Stefan-Boltzmann constant.

Having the thermal boundary conditions, heat source, and heat fluxes set, the time-domain simulations were conducted to obtain the temperature profile within the cylindrical control volume in air

and water. Fig. S1 shows the volumetric average temperature of the material under illuminations with different light intensities in water and air. Fig. S2 shows the volumetric average stored energy in the material under illuminations with different light intensities in water and air. Note that the energy conversion efficiency can be defined as the ratio between the stored energy in the material and the input energy it receives from the light source ($\eta = \frac{\dot{E}_{st}}{\dot{E}_{in}}$). Using the stored energy in air and in water, we can calculate the ratio between the energy conversion efficiency in air and water by $\frac{\eta_{Air}}{\eta_{Water}} = \frac{\dot{E}_{st}^{Air}}{\dot{E}_{st}^{Water}}$. The variation of $\frac{\eta_{Air}}{\eta_{Water}}$ $vs. I$, given in the inset in Fig. S2 shows that the energy conversion efficiency is much larger in air than water as a result of greater heat dissipation of input energy in water.

S2. Material characterization

The physiomechanical properties of LCN and LCG samples are summarized in Table S1. Each parameter is measured or calculated according to the procedure written below or in the Methods section of the main article.

Rheological Characterization:

LCGs with the higher content of 5CB became so soft that performing dynamic mechanical analysis to determine their modulus was impractical. Instead, we performed oscillatory frequency sweep rheology tests at room temperature to measure the shear modulus after in-situ curing of gels on a plate-plate geometry. The rheometer was equipped with a UV curing module that allowed in-situ cross-linking of the precursor mixtures in the testing geometry before the test. Relatively constant and higher storage modulus ($G' > G''$ and $\tan \delta < 1$) confirms the glass-like and fairly elastic behavior of all samples in the tested strain magnitude (1%) for angular frequencies up to 1000 rad s^{-1} at room temperature (Fig. S3). Limitations of our setup did not allow us to run temperature sweep tests and also investigate the anisotropic mechanical properties of samples with predefined alignment (planar, homeotropic, and splay). Instead, LCN and LCG precursors were polymerized in their nematic phase but without any preferential alignment. A more detailed study on the anisotropic mechanical behavior of the LCGs is the subject of

our future work, where a modified setup will be used in order to run rheology tests on aligned samples and at different temperatures.

Differential Scanning Calorimetry (DSC):

In order to measure the glass transition temperature (T_g) and nematic-to-isotropic T_{NI}, we monitored the variation of heat flux with temperature for LCN and LCG samples. The samples were cooled down to -80 ^{0}C and then heated up to 150 ^{0}C (for LCGs) and 200 ^{0}C (for LCN) in two consecutive cycles (10 ^{0}C min^{-1}). Fig. S4 shows the results of the second thermal cycle after erasing the thermal memory of the samples in the first cycle. Glass transition temperature of LCN has drastically reduced with the addition of 70 wt% 5CB. However, the evolution of heat flux with temperature for all samples does not show a pronounced nematic-to-isotropic transition point, but only a broad peak for LCG-70 at around 57 ^{0}C. As mentioned in the main article, the partial extinction of light in POM for temperature above 150 ^{0}C confirms the presence of residual order even at high temperatures. This is reminiscent of a smooth phase change for these samples, i.e. nematic-to-paranematic (N-PN). To get more insight into the transition behavior of LCN and LCGs, we conducted DSC in temperature modulated mode (modulation rate of 2 ^{0}C min^{-1} with 0.32 ^{0}C amplitude). As shown in Fig. 2c the evolution of C_P with temperature becomes much more pronounced around the N-PN transition by the addition of 5CB. Indeed, the transition for LCG-70 is closer to a first-order transition with a change in the slope of C_P vs T (inset in Fig. 2c). This sharp phase change eventually translates into a sharp physiomechanical transition and accordingly macroscopic deformation

Polarized Optical Microscopy:

We used polarized optical microscopy (POM) to confirm the planar alignment of samples to be used in expansion/contraction experiments (Fig. 5a-b). We also used POM with a heating stage to determine the nematic to isotropic transition temperature (T_{NI}) of the LCN and LCG precursors before and after polymerization. T_{NI} of pre-polymerized precursors were obtained during cooling (1 ^{0}C min^{-1}) of samples

which were already heated up to 100 ^{0}C (5 ^{0}C min^{-1}). Heating polymerized LCN and LCG samples to 150 ^{0}C did not lead to the full extinction of light (Fig. S5c-f).

Measuring Order Parameter:

We measured the dichroism of the dye which was doped in 5CB, LCN, and LCGs, sandwiched in planar cells with 5 μm thickness, to have an approximation of their order parameter. Cells without dyes were also prepared as reference samples. Transmission spectra were measured with a CCD camera with a built-in micro-spectrometer (PIXIS 256, Princeton Instruments) equipped with a polarization controller. A broadband light was shone on samples, once with linear polarization along the director field and once perpendicular to it. We recorded the transmission spectra $T_{\parallel}(\lambda)$ and $T_{\perp}(\lambda)$ (Fig. S6). We also measured the transmission spectra of the reference sample $T_{\parallel}^{r}(\lambda)$ and $T_{\perp}^{r}(\lambda)$. Absorption of dyes along the director field ($A_{\parallel}$) and perpendicular to it ($A_{\perp}$) are calculated from $A_{\parallel}(\lambda) = \frac{T_{\parallel}(\lambda) - T_{\parallel}^{r}(\lambda)}{T_{\parallel}^{r}(\lambda)}$ and $A_{\perp}(\lambda) = \frac{T_{\perp}(\lambda) - T_{\perp}^{r}(\lambda)}{T_{\perp}^{r}(\lambda)}$.

The order parameter *S* is related to the absorption of dye by $S_0 = \frac{A_{\parallel}(\lambda^*) - A_{\perp}(\lambda^*)}{A_{\parallel}(\lambda^*) + 2A_{\perp}(\lambda^*)} \cong S(1 - 3/2 \sin^2 \alpha)$

where λ^* is the absorption peak of the dye and α is the angle between the direction of the molecular long axis and the direction of the vibrational transition moment. Variation of S_0 with temperature was monitored by repeating the same experiment and calculation at different temperatures using a heating stage (44).

Equilibrium Swelling Ratio, Leaching and Water Uptake:

As mentioned in the main article, our samples, in fact, are plasticized LCNs that are partially swollen below their equilibrium swelling degree ($Q = \left(\frac{l^{\parallel}}{l_0^{\parallel}}\right)\left(\frac{l^{\perp}}{l_0^{\perp}}\right)^2$). Q of the LCN and LCG samples were calculated by immersing the 2×2 mm^2 samples in 5CB overnight and measuring the size of the samples parallel and perpendicular to the director field after equilibrium. Results show that LCG-70 is very close to its equilibrium swelling, which might lead to leaching (62) of 5CB during large contractions at very high temperatures (see Fig. S7 and Table S1). We also measured the leaching of 5CB from LCG-70 samples when conditioned in water for different time periods (1 hr to 72 hrs). We exposed one of the

samples, conditioned for 72 hrs, to light with similar intensity and wavelength to that used in underwater locomotion experiments, for 15 minutes. We weighted the samples before conditioning in water and after complete drying for one week in ambient condition. Results showed a maximum of ~1.2% weight reduction, which can mainly be attributed to the 5CB leaching. Exposure to light did not cause larger weight reduction. Measuring the exact amount of water uptake is very challenging both in immersed conditions and after one week of drying. However, given the low amount of weight reduction after complete drying, we believe that the water uptake by the LCG during the conditioning is negligible.

S3. Density change experiments

The density change of isotropic and splay LCG-70 constructs upon illumination with light was measured by submerging 2 × 2 mm^2 samples in brines of salt-water with different densities ranging from 1 to 1.25 g cm^{-3}. The initial density of both samples was almost equal and about 1.102 g cm^{-3}, which lead to sinking the samples in brines with densities of less than this value. We illuminated both samples with the same light source and observed the floatation of only splay LCG-70 in brines with densities down to 1.021±0.008 g cm^{-3}. Accordingly, the maximum density reduction for splay LCG-70 was ~ 8%. The isotropic sample did not float in any of the experiments upon illumination (see Fig. S8). It is worth noting that previous studies show that the temperature of the derivatives of DR1A can reach 200 ^{0}C upon exposure to proper lights at dry conditions (30, 63). Such a temperature gradient might lead to the formation of bubbles around the heating object immersed in liquids. Except for experiments that were conducted by 532 nm laser at maximum light intensities (Fig. 3a), we avoided the formation of large bubbles around our samples by maintaining illumination at lower intensities. Albeit, merely visual inspection cannot rule out the formation of micro-bubbles at the point of exposure. While we are not confident in this matter, the formation of micro-bubbles can also play a positive role in the increase of buoyancy and thrust. Indeed, swimming based on bubble formation or purely physical density change has been recently the subject of study in several reports (64, 65).

S4. Modeling of thermomechanical response

The thermomechanical response of splay LCN and LCG beams were separately modeled in the Solid Mechanics module of COMSOL Multiphysics 5.4. A hyperelastic neo-Hookian material model was used for the splay beam(58). We assumed the Poisson's ratio of $\nu = 0.49$ for the LCG and LCN beams, and thus the bulk modulus K was related to shear modulus G' by $K = \frac{2(1+\nu)}{3(1-2\nu)} G'$. For the mechanical deformation of the heated beam, an anisotropic thermal strain distribution along the beam thickness was given as an external strain field. Note that for predicting the bending behavior of splay beams, we assumed that the modulus of elasticity of the material is isotropic(59). The total strain on the heated or illuminated sample in the tensor format can be expressed by:

$$\varepsilon_{ij}^{total} = \varepsilon_{ij}^{M} + \varepsilon_{ij}^{th}, \quad i,j = 1,2,3 \,, \tag{S4}$$

where, ε_{ij}^{M} and ε_{ij}^{th} are the mechanical and thermal strains, respectively. By decomposing the thermal strain from the nematic director frame into the laboratory frame (xyz in Fig. S9), and assuming plane stress conditions for thin cantilever beams ($\sigma_{yy} = 0$), the thermal strains in x, and z directions can be written as (59) :

$$\varepsilon_{z}^{th} = \varepsilon_{\perp}$$

$$\varepsilon_{x}^{th} = \varepsilon_{\perp} \sin^2\theta + \varepsilon_{\parallel} \cos^2\theta \tag{S5}$$

θ is the angle between the nematic director and the planar director field and was assumed to linearly change throughout the thickness by $\theta = \frac{\pi}{4}(1 + \frac{y}{h})$. Experimental thermal strain data was fitted to 4th-degree polynomial functions (Fig. S10 and Table S2).

In order to simulate the thermomechanical response of the LCN and LCG cantilevers under local light exposure (Fig. 3a), we have assumed an external thermal strain field at a region of interest. Since the external strain data were obtained from equation S4, the final mechanical deformation was correlated directly to the temperature. The tip displacement of the cantilever beams versus temperature is shown in Fig. S11. It is evident that the maximum tip deflection is the largest for LCG-70, indicating that a lower

temperature difference is required to achieve a noticeable bending deformation. Moreover, the light intensity could be readily correlated to the local temperature profile of the beams by comparing the deformation data from the experimental and simulation data.

S5. Calculation of the swimming metrics

In order to estimate the Reynolds number of our LCG during swimming, we used two definitions for the Reynolds number. The first *Re* is calculated based on the whole LCG body and calculated by $Re_{\mathrm{B}} = \frac{\bar{V}L(t)}{\nu}$, where $\bar{V}$ is the average velocity during the upward locomotion (~ 4.9 mm s^{-1}), L is the projected length normal to the locomotion direction ($4.5 < L < 14.2$), and ν is the kinematic viscosity of the medium (~ 10^{-6} m^2 s^{-1}). As a result, $22 < Re_{\mathrm{B}} < 78.4$. The second *Re* is calculated based on the propulsion in the vicinity of the LCG end-point by $Re_{\mathrm{L}} = \frac{uw}{\nu}$, where w is the width of the bending LCG (~ 3 mm). u is the speed by which the LCG end-points move toward each other during the stroke period. This velocity is calculated by tracking the center of the mass and end-points of the LCG over time ($u \approx 7.43$ mm s^{-1}). Hence, $Re_{\mathrm{L}} \approx 22.3$. The Stokes number (*Stk*) is calculated by $Stk = 2\pi l^2/T\nu$, which is calculated based on the body length and the pitching velocity of the body (41).

The swimming takes place when net forces in the upward direction, i.e. buoyancy (F_B) and thrust (F_T), overcome the gravity (F_W) and Drag (F_D). The force balance on the undulating LCG can be expressed as $\sum F = F_T + F_B - F_W - F_D = ma$. As the velocity during the heave is almost constant (Fig. 5c), we can assume that $\sum F = F_T + F_B - F_W - F_D = 0$. Moreover, the illumination of LCG results in the reduction of its density to the point where buoyancy is almost equal to the weight. Therefore, the force balance equation will be reduced to $F_T \cong F_D$. In order to calculate the thrust, we assume that the upward locomotion of our LCG is achieved by drag-based paddling or viscous rowing (66). The net upward thrust is produced as long as the drag acting on the paddle during the power stroke is greater than during the relaxation (67). In such a case, the drag force acting on each side of our bent LCG determines the thrust created during the stroke. This drag force can be calculated by $F_D \cong \frac{1}{2}\rho_m u^2 A C_D$. In this correlation, ρ_m is

the density of the liquid medium (~ 1.03 g cm^{-3}), u is the instantaneous velocity of our LCG obtained by tracking the center and end-points over-time (~ 7.3 mm s^{-1}), and A is the projected surface area (~ 24 mm^2), and C_D is the drag coefficient. We assume that $1 < C_D < 2$. Therefore, 1.16×10^{-7} N $< F_T < 2.32 \times 10^{-7}$ N.

Table S1 Physiomechanical properties of synthesized LCN and LCGs.
† These parameters were measured at room temperature 23 ^{o}C.

Sample	T_{NI} (^{o}C) of pre-polymerized precursors	T_g (^{o}C)	$^{\dagger}\rho$ (g cm^{-3})	†G' (kPa)	$^{\dagger}Q$
LCN	59.6±1.5	9.7±0.5	1.192	1400.36	2.46
LCG-30	53.9±2	-25±1.2	1.159	642.2	1.82
LCG-50	47.5±1.5	-44±0.5	1.130	116.4	1.36
LCG-70	40.6±1.2	-59±0.8	1.102	29.2	1.11
5CB	35.4	-	1.008	-	-

Table S2 The curve fit formulas extracted from the experimental thermal strain data

Sample	$\varepsilon_{\parallel}$	$\varepsilon_{\perp}$
LCN	$8.049\times10^{-10}T^4 - 6.643\times10^{-8}T^3$ $- 1.21\times10^{-5}T^2 + 9.947\times10^{-4}T - 1.53\times10^{-2}$	$1.231\times10^{-9}T^4 - 4.951\times10^{-7}T^3$ $+ 5.697\times10^{-5}T^2 - 2.152\times10^{-3}T$ $+ 2.476\times10^{-2}$
LCG-30	$-1.002\times10^{-9}T^4 - 2.827\times10^{-7}T^3$ $+ 6.766\times10^{-5}T^2 - 4.01574165\times10^{-3}T$ $+ 6.348\times10^{-2}$	$7.480\times10^{-9}T^4 - 1.679\times10^{-6}T^3$ $+ 1.289\times10^{-4}T^2 - 3.780\times10^{-1}T$ $+ 3.762\times10^{-2}$
LCG-50	$2.237\times10^{-9}T^4 - 1.031\times10^{-6}T^3$ $+ 1.261\times10^{-4}T^2 - 6.452\times10^{-3}T$ $+ 9.558\times10^{-2}$	$3.532\times10^{-9}T^4 - 7.499\times10^{-7}T^3$ $+ 5.303\times10^{-5}T^2 - 8.005\times10^{-4}T$ $- 2.230\times10^{-3}$
LCG-70	$2.162\times10^{-8}T^4 - 4.532\times10^{-6}T^3$ $+ 3.289\times10^{-4}T^2 - 1.119\times10^{-2}T$ $+ 1.349\times10^{-1}$	$-4.107\times10^{-8}T^4 + 9.247\times10^{-6}T^3$ $- 7.148\times10^{-4}T^2 + 2.326\times10^{-2}T$ $- 2.632\times10^{-1}$

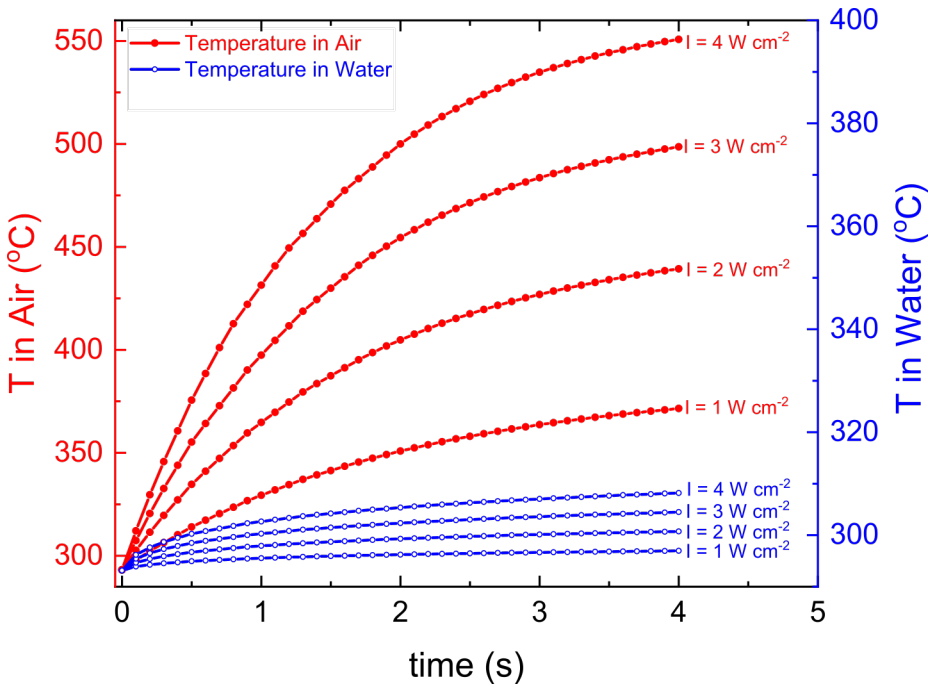

Fig. S1. Finite-element simulation results for the modeling of photothermal heating of the native LCN; graphs show the variation of temperature with time for light with different intensities.

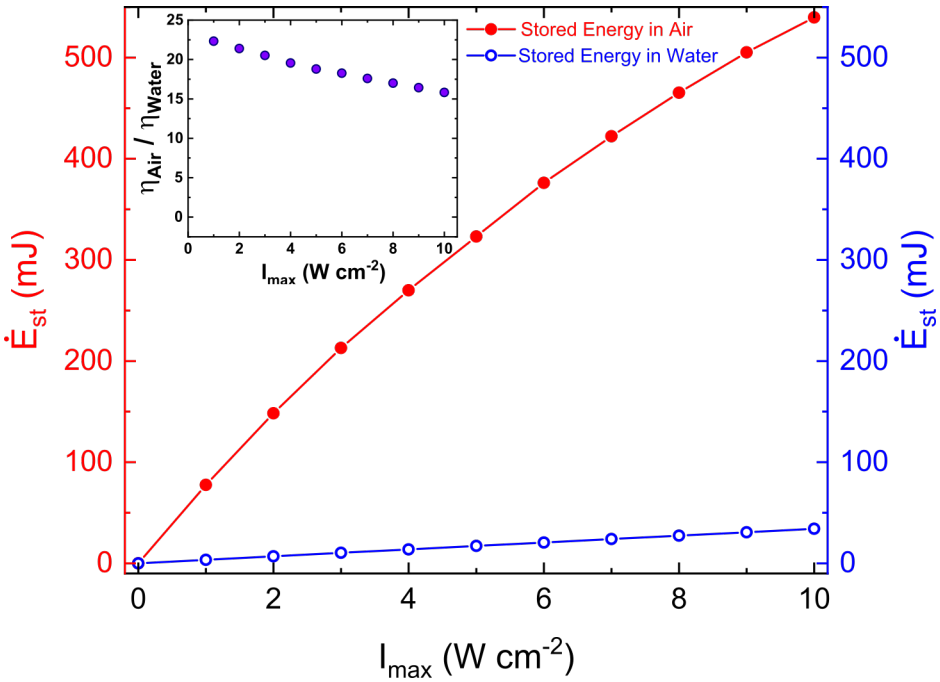

Fig. S2. Finite-element results for the modeling of photo-thermal heating of the native LCN; graphs show the variation of stored energy with the intensity of light. The inset shows the variation of the ratio between the energy conversion efficiency in air and water with the input intensity of light.

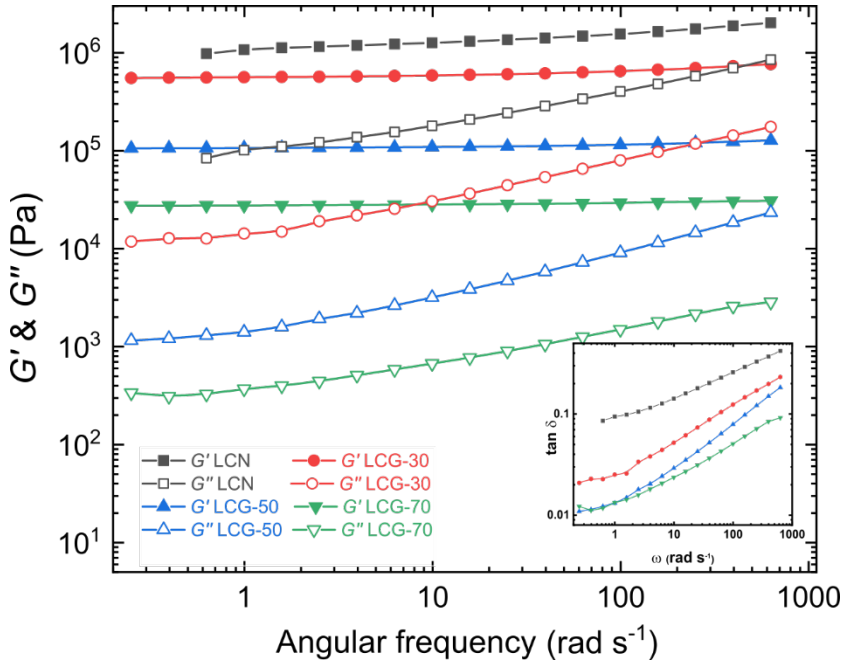

Fig. S3. Storage and loss modulus of in-situ prepared polydomain LCN and LCG constructs under oscillation with angular frequency from 0.1 to 1000 rad s^{-1} at room temperature; the inset shows the variation of tanδ by angular frequency.

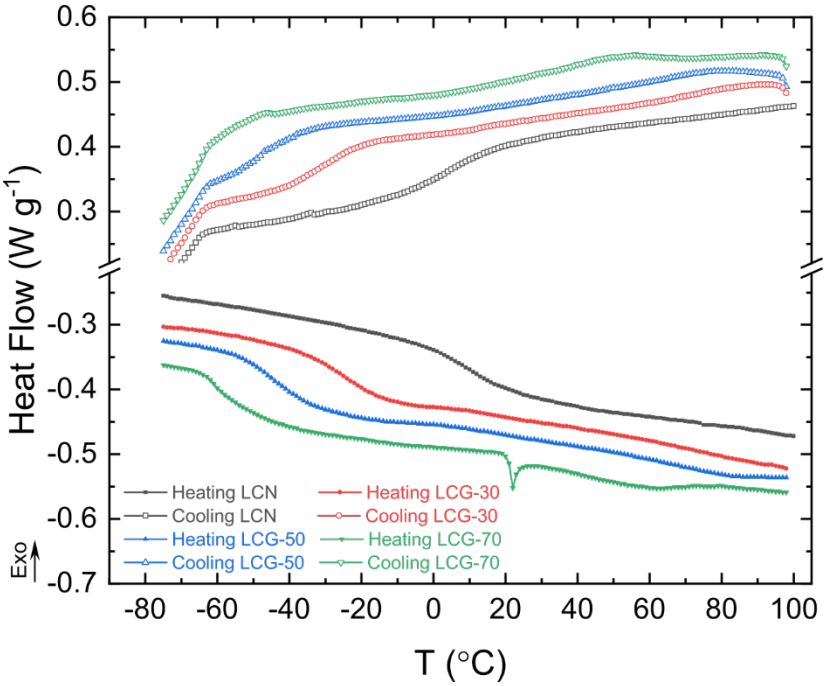

Fig. S4. DSC characterization results showing the variation of heat flux with temperature for different samples.

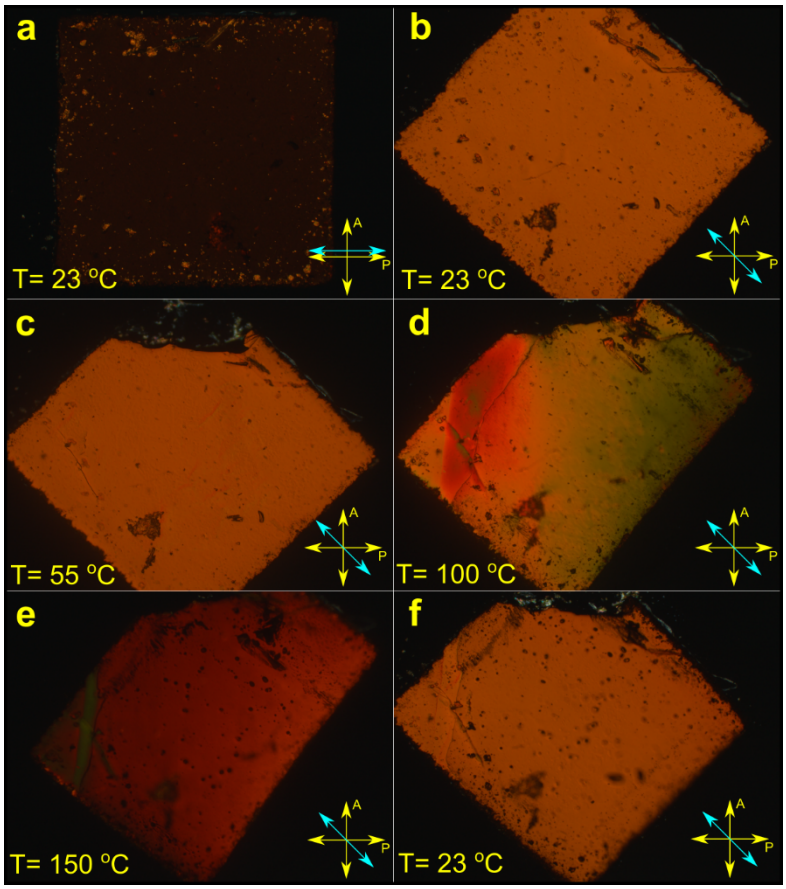

Fig. S5. POM images of a planar LCG-70 construct under crossed polarizers at room and elevated temperatures; in **a**, the sample is parallel to and in **b**, the sample is 45^{o} rotated with respect to polarizers. **c-e** show the POM during the heating of the sample up to 150 ^{o}C and **f** shows when the sample is cooled down to the room temperature.

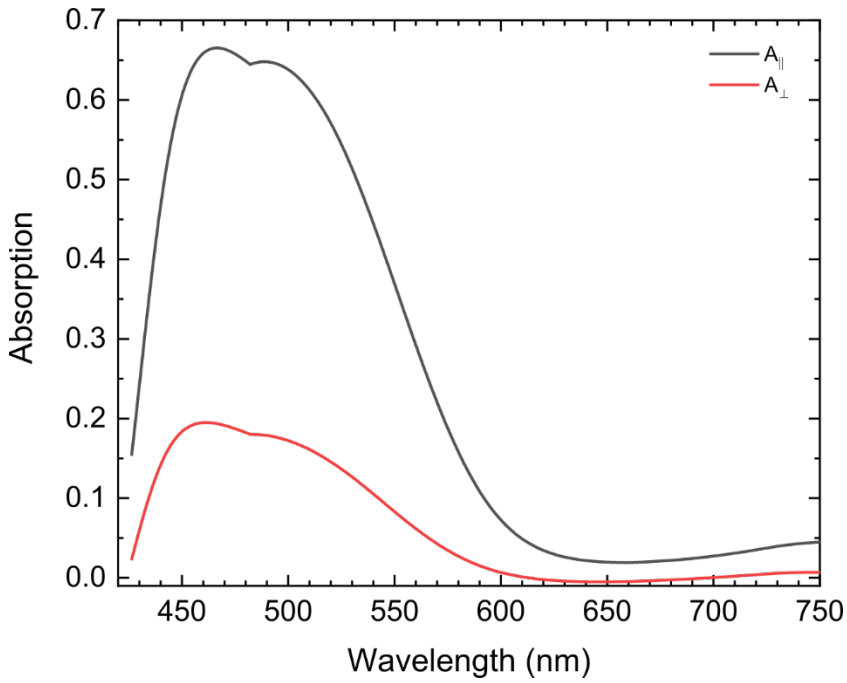

Fig. S6. Absorption spectra obtained by the illumination of an LCN sample with a linearly polarized broadband light parallel and perpendicular to its optical axis.

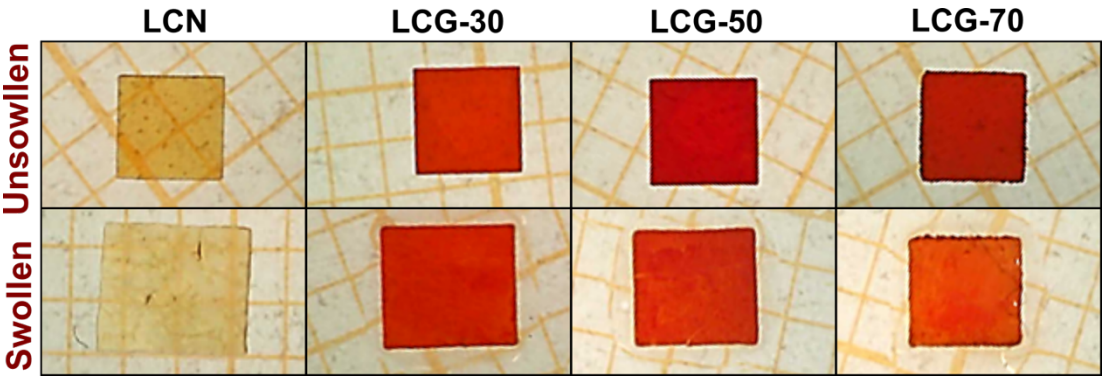

Fig. S7. Swelling of planar LCN and LCG samples in 5CB overnight; LCN has the highest swelling ratio and LCG-70 has the lowest. The swelling perpendicular to the nematic director is larger than that of parallel to it.

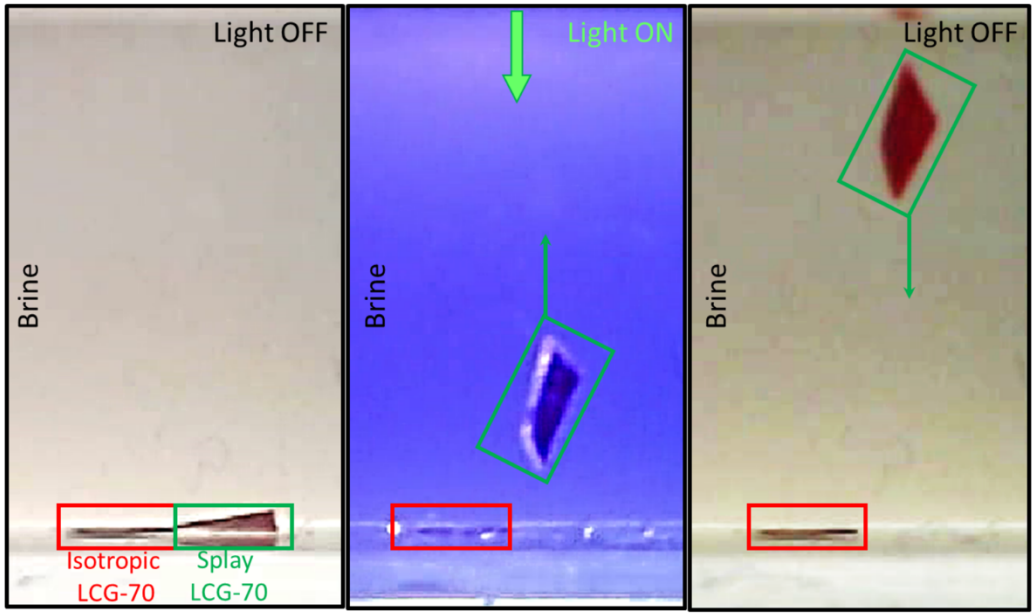

Fig. S8. Illumination of an isotropic and a splay LCG-70 sample (2 × 2 mm^2) in salt-water brine (ρ = 1.03 g cm^{-3}); results show instant flotation of the splay LCG-70, whereas the isotropic LCG-70 does not float even under prolonged exposure to the light.

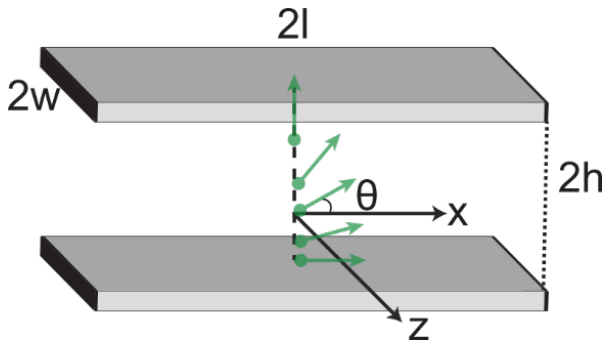

Fig. S9. The schematic view of a beam with splay alignment, where the nematic director linearly rotates from the bottom (y = -h) to the top (y = h).

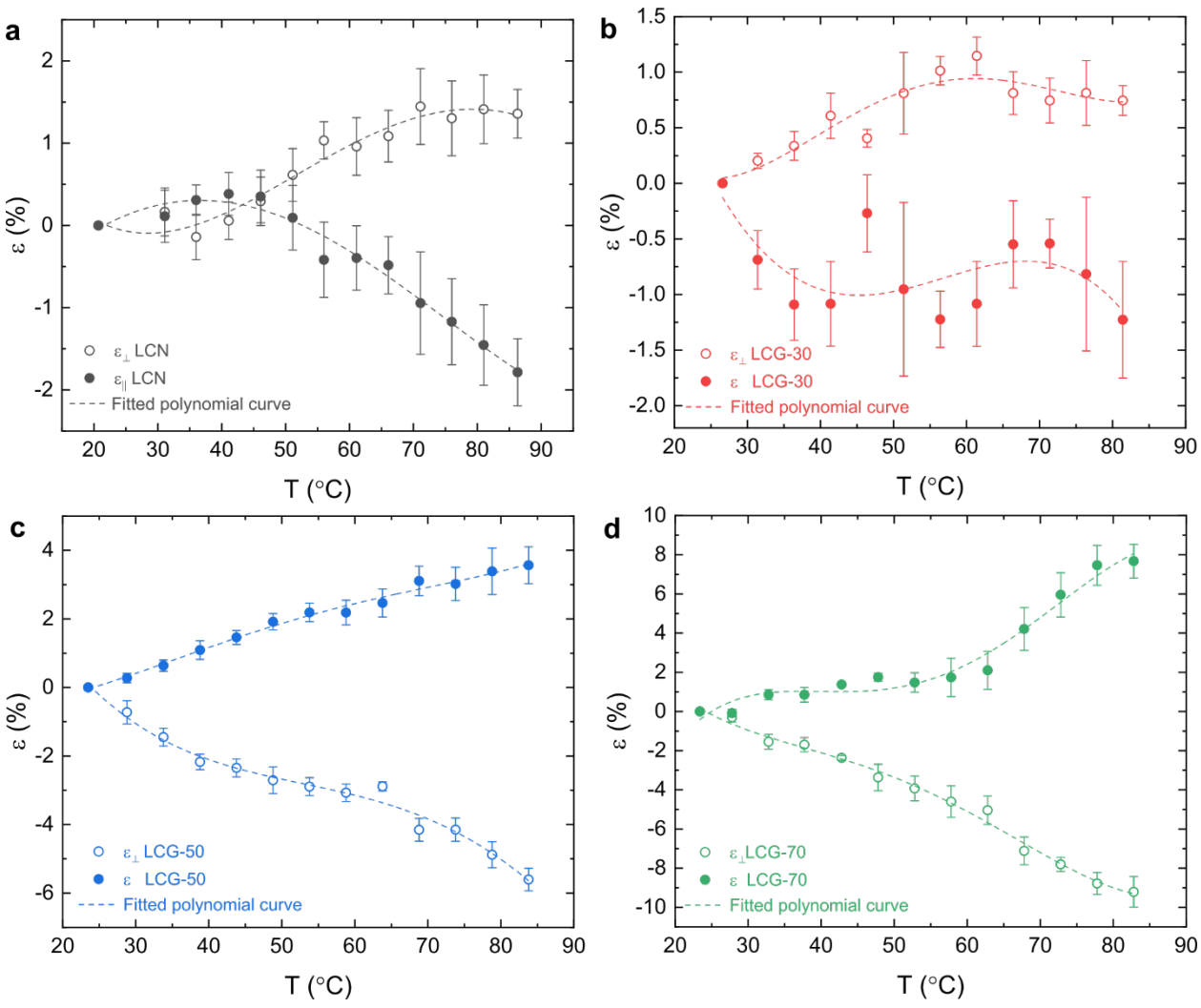

Fig. S10. The thermal strain versus temperature profiles for **a** LCN, **b** LCG-30, **c** LCG-50, and **d** LCG-70; markers present the experimental data for strain parallel and perpendicular to the director, and the dashed lines represent the 4th-degree polynomial fit.

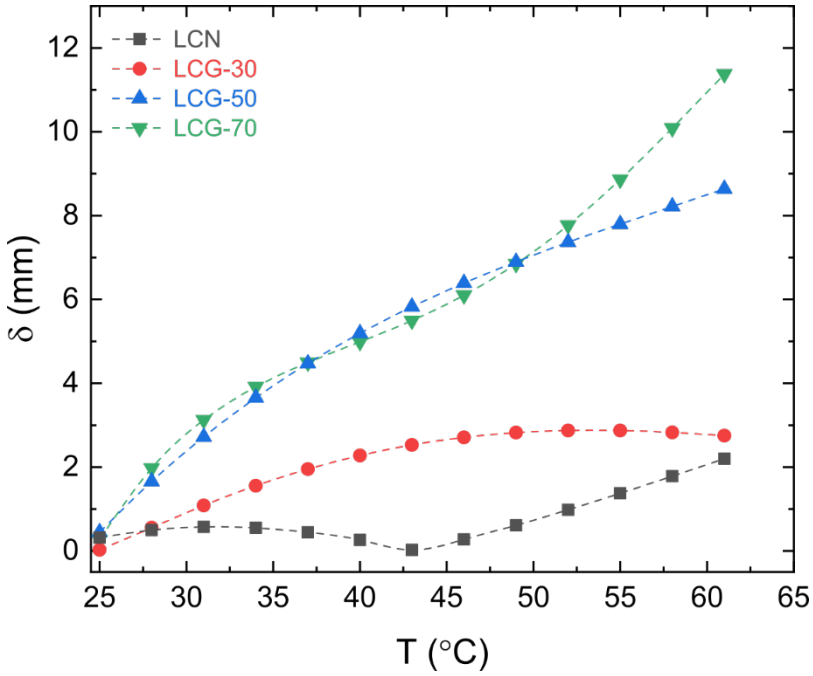

Fig. S11. Finite-element simulation results for the variation of tip displacement with temperature induced by the photothermal heating of samples

Supplementary Movies

Movie S1. Photothermal actuation of planar LCN and LCG constructs; samples were illuminated by a 532 nm laser in room temperature water. The sample size is $1 \times 1 \times 0.1$ mm^3. The playback speed is 1X.

Movie S2. Photothermal bending oscillation of LCN and LCG cantilevers; samples were illuminated by a 532 nm laser at different frequencies in room temperature water. The sample size is $9 \times 1.5 \times 0.1$ mm^3. The playback speed is 1X.

Movie S3. Making waves by constant illumination of LCN and LCG constructs; samples were illuminated by an arc lamp in room temperature water. The sample size is $21 \times 3 \times 0.1$ mm^3. The two ends are clamped with a 16 mm distance. The playback speed is 1X.

Movie S4. Framed locomotion of the LCG-50 construct; the sample was illuminated by 532 nm laser in room temperature water. The sample size is $21 \times 3 \times 0.1$ mm^3. The two ends are clamped with a 16 mm distance. The playback speed is 1X. The animation shows the simulation results for the photothermal formation of waves in a passive frame.

Movie S5. Underwater walking of the LCG-50 construct on a ratchet surface; the sample was illuminated by an arc lamp in room temperature water. The sample size is $21 \times 3 \times 0.1$ mm^3. The playback speed is 1X.

Movie S6. Underwater jumping of the LCG-70 construct on a ratchet surface; the sample was illuminated by an arc lamp in room temperature water. The sample size is $21 \times 3 \times 0.1$ mm^3. The playback speed is 1X.

Movie S7. Underwater jumping of the LCG-70 construct on a smooth surface; the sample was illuminated by a 532 nm laser in room temperature water. The sample size is $21 \times 3 \times 0.1$ mm^3. The playback speed is 1X.

Movie S8. Underwater swimming of the LCG-70 construct; the sample was illuminated by an oscillatory light from an arc lamp in room temperature salt/water brine of 1.03 g cm^{-3} density. The sample size is 16 × 3 × 0.1 mm^3. The playback speed is 1X.

References

1. J. E. Marshall, E. M. Terentjev, Photo-sensitivity of dye-doped liquid crystal elastomers. *Soft Matter* **9**, 8547–8551 (2013).
2. F. P. Incropera, D. P. De Witt, Fundamentals of heat transfer. (1981).
3. A. H. Gelebart, *et al.*, Photoresponsive Sponge-Like Coating for On-Demand Liquid Release. *Adv. Funct. Mater.* **28**, 1–8 (2018).
4. J. Vapaavuori, A. Laventure, C. G. Bazuin, O. Lebel, C. Pellerin, Submolecular Plasticization Induced by Photons in Azobenzene Materials. *J. Am. Chem. Soc.* **137**, 13510–13517 (2015).
5. T. Luan, *et al.*, Bubble-Enabled Underwater Motion of a Light-Driven Motor. *Small* **15**, 1–7 (2019).
6. M. Song, *et al.*, Biomimicking of a Swim Bladder and Its Application as a Mini-Generator. *Adv. Mater.* **29**, 10–13 (2017).
7. K. E. Feitl, A. F. Millett, S. P. Colin, J. O. Dabiri, J. H. Costello, Functional Morphology and Fluid Interactions During Early Development of the Scyphomedusa Aurelia aurita. *Biol. Bull.* **217**, 283–291 (2009).
8. T. Blough, S. P. Colin, J. H. Costello, A. C. Marques, Ontogenetic Changes in the Bell Morphology and Kinematics and Swimming Behavior of Rowing Medusae: The Special Case of the Limnomedusa Liriope tetraphylla. *Biol. Bull.* **220**, 6–14 (2011).